

# Efficient flexible dye-sensitized solar cells from rear illumination based on different morphologies of titanium dioxide photoanode

Zhe He<sup>1</sup>, Gentian Yue<sup>1,2,†</sup>, Yueyue Gao<sup>1</sup>, Chen Dong<sup>1</sup>, and Furui Tan<sup>1,†</sup>

<sup>1</sup>School of Future Technology and Henan Key Laboratory of Photovoltaic Materials, Henan University, Kaifeng 475004, China

<sup>2</sup>Zhenjiang Mars Photoenergy Technology Co., Ltd, Zhenjiang 212011, China

**Abstract:** The TiO<sub>2</sub> with nanoparticles (NPs), nanowires (NWs), nanorods (NRs) and nanotubes (NTs) structures were prepared by using a *in-situ* hydrothermal technique, and then proposed as a photoanode for flexible dye-sensitized solar cell (FDSSC). The influences of the morphology of TiO<sub>2</sub> on the photovoltaic performances of FDSSCs were investigated. Under rear illumination of 100 mW·cm<sup>-2</sup>, the power conversion efficiencies of FDSSCs achieved 6.96%, 7.36%, 7.65%, and 7.83% with the TiO<sub>2</sub> photoanodes of NPs, NWs, NRs, and NTs and PEDOT counter electrode. The FDSSCs based on TiO<sub>2</sub> NRs and NTs photoanodes have higher short circuit current densities and power conversion efficiencies than that of the others. The enhanced power conversion efficiency is responsible for their nanotubes and rod-shaped ordered structures, which are more beneficial to transmission of electron and hole in semiconductor compared to the TiO<sub>2</sub> nanoparticles and nanowires disordered structure.

**Key words:** dye-sensitized solar cells; photoanode; TiO<sub>2</sub>; morphology

**Citation:** Z He, G T Yue, Y Y Gao, C Dong, and F R Tan, Efficient flexible dye-sensitized solar cells from rear illumination based on different morphologies of titanium dioxide photoanode[J]. *J. Semicond.*, 2024, 45(2), 022801. <https://doi.org/10.1088/1674-4926/45/2/022801>

## 1. Introduction

Dye-sensitized solar cells (DSSCs) with economy, environmental friendliness, mechanical stability, simple preparation process, and high efficiency of 14%, are considered as a favorable choice compared to the silicon device<sup>[1–3]</sup>. As an important component of DSSC, photoanode is not only a support and adsorption carrier for dye molecules, but also an electron transport carrier. Titanium dioxide (TiO<sub>2</sub>) is the most representative for its rich optical, dielectric, catalytic, and antimicrobial properties, which leads to a variety of uses in solar cells, photocatalytic, and fuel cells<sup>[4–7]</sup>. Among three polymorphs of rutile, anatase, and brookite, rutile TiO<sub>2</sub> has more stable physicochemical properties, higher refractive index and light-scattering capability compared to anatase<sup>[8–10]</sup>. Also, the morphology of TiO<sub>2</sub> shows significant effect on its physical and chemical properties, such as the one-dimensional (1-D) structure, whose charge transport is preferred compare to the mesoporous structure due to the reduction in grain boundaries and lattice imperfections, thereby slowing down the electron hole recombination rate and accelerating electron transfer, and helping to improve the performance of various optoelectronic applications<sup>[11–13]</sup>. Sadhu *et al.* reported the fabrication of a three-dimensional (3-D) rutile-phase TiO<sub>2</sub> microsphere arrays on fluorine-doped conducting oxide (FTO), and showed superior photon-harvesting performance owing to the increase in light-scattering in DSSC<sup>[14]</sup>. Ri *et al.* spot-

lighted growth of a sea urchin-like rutile TiO<sub>2</sub> hierarchical microsphere on Ti foil, which showed much better light-scattering capability in visible region than the bare Ti foil<sup>[15]</sup>. Sun *et al.* recorded a bilayer DSSC with an efficiency of 7.2% based on a bilayer TiO<sub>2</sub> film consisting of a 1-D nanowire arrays as underlayer and a 3-D dendritic microsphere as light-scattering overlayer<sup>[16]</sup>. These results indicate that designing DSSC photoanodes with different morphologies is of great significance for improving the performance of DSSC.

Moreover, the substrate of traditional DSSC is FTO, and its features of rigid and heavy can not meet all application scenarios<sup>[17]</sup>. To solve this issue, some flexible substrates (e.g., ITO/PET, ITO/PEN and metals) are used to replace FTO glass. Nevertheless, the ITO/PET and ITO/PEN substrates are high-cost and intolerant of temperatures higher than 150 °C, which is much lower than the temperature required for manufacturing photoanodes on FTO glass (450–500 °C), thus resulting in the relatively poor performance of plastic-based DSSCs. Therefore, high-temperature resistant metal foils (such as Ti and stainless steel) are used to fabricate flexible DSSCs (FDSSCs) with encouraging performance compared with the plastic-based ones<sup>[18, 19]</sup>.

In this contribution, the anatase phase TiO<sub>2</sub> with four morphologies of nanoparticles, nanowires, nanorods and nanotubes (abbreviated as NP, NW, NR and NT) were prepared by using a *in-situ* hydrothermal synthesis and served as photoanode in FDSSCs. The influences of the morphology of TiO<sub>2</sub> on the adsorption capacity of dyes and charge transfer performances of FDSSCs were extensively investigated. The power conversion efficiencies of the FDSSCs based on NP, NW, NR, and NT TiO<sub>2</sub> photoanodes and poly (3,4-ethylenedioxythiophene) (PEDOT) counter electrode reached 6.96%, 7.36%,

Correspondence to: G T Yue, [yuegentian@126.com](mailto:yuegentian@126.com); F R Tan, [frtan@henu.edu.cn](mailto:frtan@henu.edu.cn)

Received 31 AUGUST 2024; Revised 28 OCTOBER 2024.

©2024 Chinese Institute of Electronics

7.65%, and 7.83%, respectively under rear illumination of  $100 \text{ mW}\cdot\text{cm}^{-2}$  and the optimized condition.

## 2. Experimental

### 2.1. Various $\text{TiO}_2$ photoanode preparation

A reserved thin  $\text{TiO}_2$  blocking layer was prepared by immersing the Ti substrate in 0.15 M of  $\text{TiCl}_4$  isopropanol solution for 12 h, followed by sintering at  $450^\circ\text{C}$  for 30 min in air.

Next, four  $\text{TiO}_2$  photoanodes with different morphologies were prepared.

(1)  $\text{TiO}_2$  NPs paste were prepared as described previously<sup>[20–22]</sup>.

(2)  $\text{TiO}_2$  NRs were prepared as following<sup>[23–25]</sup>. 5 mL Tetra-butyltitanate was rapidly added to 75 mL absolute ethyl alcohol under stirring for 0.5 h and followed by addition of 0.33 mL concentrated sulfuric acid and 0.3 mL deionized water to the solution, and then transferred into 100 mL Teflon-liner and autoclaved at  $180^\circ\text{C}$  for 4 h to form a milky white slurry. The slurry was dissolved into 50 mL, 10 M NaOH solution. After ultrasonication and stirring for 0.5 h until a homogeneous solution was achieved and then the obtained solution was transferred into Teflon-liner and autoclaved at  $150^\circ\text{C}$  for 24 h. The precipitate was collected by filter and washed with distilled water and 0.3 M HCl for 3 times, followed by washing with distilled water some times and annealing at  $450^\circ\text{C}$  for 1 h.

(3)  $\text{TiO}_2$  NTs were prepared in a two-steps hydrothermal method<sup>[26, 27]</sup>. 3 g P25 powder was added into 10 M NaOH solution and then transferred into 100 mL Teflon-liner and autoclaved at  $160^\circ\text{C}$  for 4 h and  $110^\circ\text{C}$  for 20 h, respectively. After that, the obtained produce was washed with distilled water and HCl aqueous solution ( $\text{pH} = 2$ ), and then with distilled water for several times until the pH is 7. The products were calcined at  $400^\circ\text{C}$  in air for 1 h. Thus the  $\text{TiO}_2$  NTs were obtained.

The  $\text{TiO}_2$  NRs and NTs paste were prepared including of 10 mL absolute ethyl alcohol, 5 mL N-methyl-2-pyrrolidone, 0.1 g polyvinylidene fluoride, 1 g  $\text{TiO}_2$  NRs and NTs kept stirring for 12 h at  $50^\circ\text{C}$ . Soon afterwards, the  $\text{TiO}_2$  NPs, NRs, and NTs films were coated onto the preprepared blocking layer by using doctor blade method, and then sintered at  $450^\circ\text{C}$  for 30 min in air.

(4)  $\text{TiO}_2$  NWs photoanode were prepared as the reported<sup>[28–30]</sup>. 10 mL dioxane and 1 mL HCl with concentrated of 35% were mixed with stirring, and then added 1 mL titanium butoxide and  $\text{TiCl}_4$  to above solution. The obtained solution was transferred into a 25 mL Teflon-liner. The Ti substrate with a thin  $\text{TiO}_2$  blocking layer was placed into above solution at an angle against the wall, and the hydrothermal synthesis was conducted at  $180^\circ\text{C}$  for 6 h. The  $\text{TiO}_2$  NWs photoanode was obtained.

At last, the dye was loaded by immersing the bilayer  $\text{TiO}_2$  photoanodes in 0.3 mM of N719 ethanol solution for 12 h. Thus the flexible dye-sensitized  $\text{TiO}_2$  photoanodes with thickness of  $4\text{--}5 \mu\text{m}$  was obtained.

### 2.2. Fabrication of FDSSCs

The PEDOT counter electrode (CE) was electropolymerization from the base polymerization solution consisted of 0.1 M EDOT, 0.1 M  $\text{LiClO}_4$  and PEG-600 dissolved in anhydrous

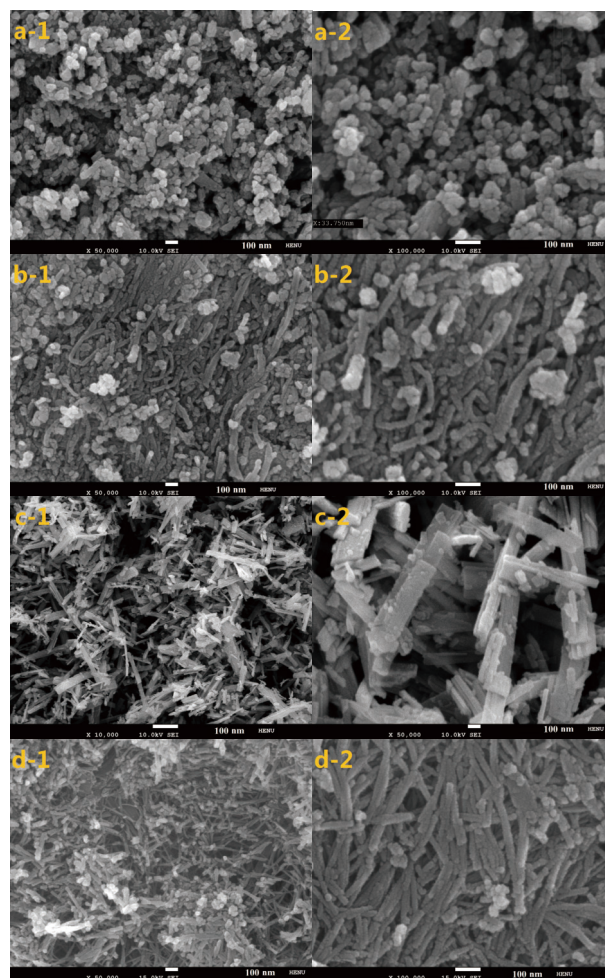


Fig. 1. SEM images of  $\text{TiO}_2$  (a) NPs, (b) NWs, (c) NRs, and (d) NTs.

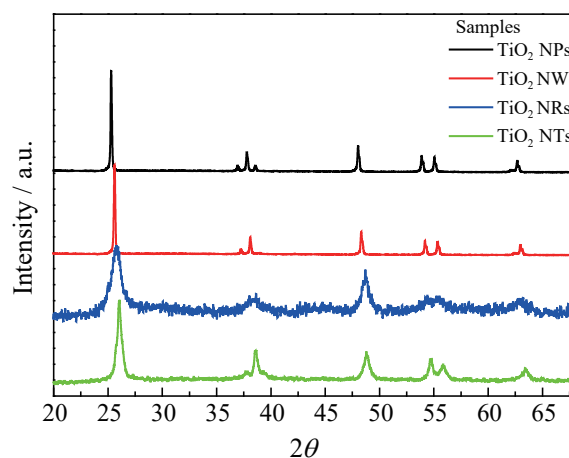


Fig. 2. (Color online) XRD patterns of  $\text{TiO}_2$  NPs, NWs, NRs, and NTs.

ethanol. The FDSSCs assembled by clipping the dye-sensitized  $\text{TiO}_2$  photoanode and Pt CE, and the liquid electrolyte consisted of 0.05 M of iodine, 0.1 M of lithium iodide, 0.6 M of tetrabutylammonium iodide and 0.5 M of 4-tert-butyl-pyridine in acetonitrile was injected in the aperture between the two electrodes.

### 2.3. Characterization

The morphology, microstructure and the elements of the samples were investigated by the transmission electron microscopy (TEM, JEM-2100F, Japan) equipped with energy dispersive spectrometer (EDS) and the field emission scanning

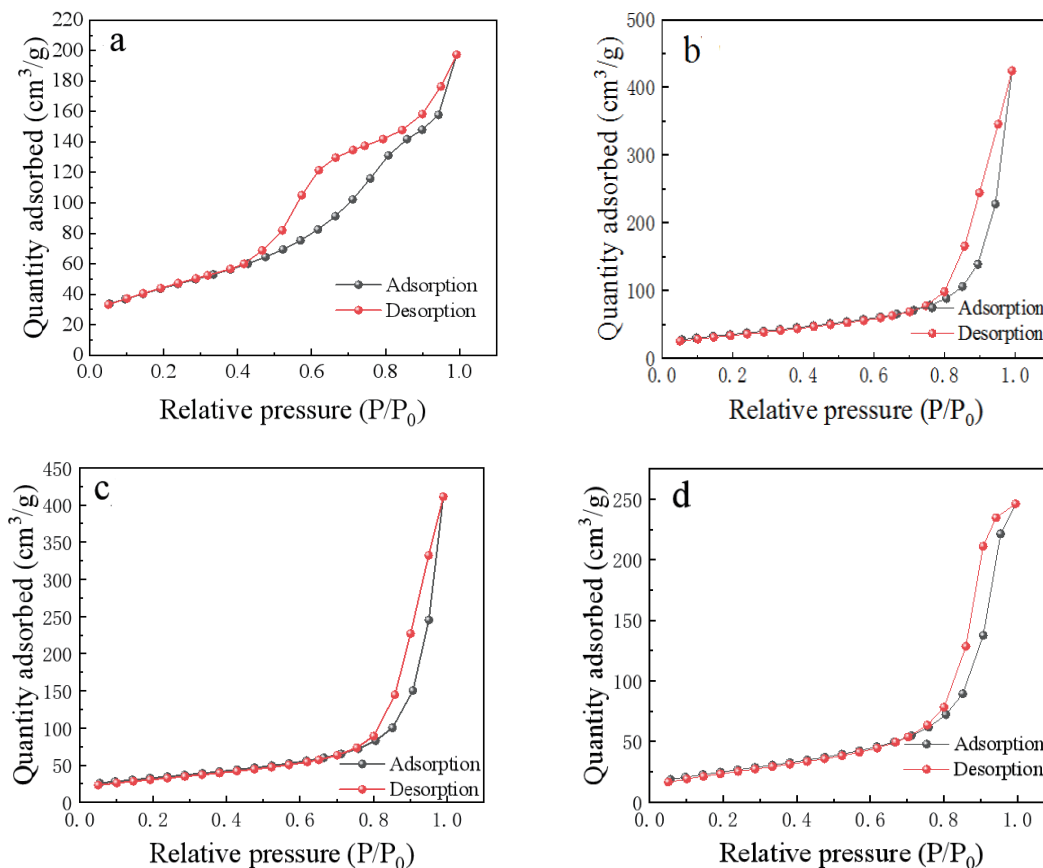


Fig. 3. (Color online) Absorption-desorption isotherm of the TiO<sub>2</sub> (a) NTs, (b) NRs, (c) NWs, and (d) NPs.

Table 1. The absorption-desorption isotherm values of the TiO<sub>2</sub> with different morphologies.

Samples	NPs	NWs	NRs	NTs
Specific surface area (m <sup>2</sup> /g)	91.9122	116.6744	126.3625	158.8077

electron microscopy (SEM, JSM-7001F, Japan). The crystalline structures of the composites were investigated by glancing incident X-ray diffractometer (X'Pert Pro, PANalytical B.V., Netherlands). The photovoltaic tests of FDSSCs with an exposed area of 0.2 cm<sup>2</sup> were carried out by measuring photocurrent-photovoltage ( $J$ - $V$ ) characteristic curves under rear irradiation of 100 mW·cm<sup>-2</sup> from the solar simulator (CEL-S500, Beijing China Education Au-light Co., Ltd) in ambient atmosphere.

### 3. Results and discussions

Fig. 1 shows the SEM images of the TiO<sub>2</sub> NPs, NWs, NRs, and NTs. Figs. 1(a)-1 and 1(a)-2 present the porous and loose nanostructure of TiO<sub>2</sub> NPs, and the Figs. 1(b)-1 and 1(b)-2 exhibit a mixture of TiO<sub>2</sub> NWs and NPs, which are beneficial for the charge transfer and electrolyte loading. To compare the effect of the TiO<sub>2</sub> morphology on electron transfer, TiO<sub>2</sub> NRs and NTs were prepared and as shown as in Figs. 1(c) and 1(d). From Figs. 1(c)-1 and 1(c)-2, the TiO<sub>2</sub> NRs with different sizes and lengths can be observed clearly. Compared to TiO<sub>2</sub> NRs, TiO<sub>2</sub> NTs with a similar size and length are shown in Figs. 1(d)-1 and 1(d)-2. In a word, the TiO<sub>2</sub> photoanode with nano-structure provides highly effective contact between the CE and the  $I^-/I_3^-$  redox couple electrolyte, thus possibly absorbing more liquid electrolyte and improving the penetration of  $I^-/I_3^-$  liquid electrolyte within TiO<sub>2</sub> film, and expecting to

obtain an excellent performance for FDSSC.

Fig. 2 displays the XRD patterns of the TiO<sub>2</sub> NPs, NWs, NRs, and NTs photoanode. From Fig. 2, the characteristic peaks for the TiO<sub>2</sub> NPs ( $2\theta = 25.3^\circ, 37.8^\circ, 48.0^\circ, 53.8^\circ, 55.1^\circ,$  and  $62.6^\circ$ ), TiO<sub>2</sub> NWs ( $2\theta = 25.5^\circ, 38.1^\circ, 48.3^\circ, 54.2^\circ, 55.3^\circ,$  and  $63.0^\circ$ ), TiO<sub>2</sub> NRs ( $2\theta = 25.7^\circ, 38.4^\circ, 48.7^\circ, 54.3^\circ, 55.5^\circ,$  and  $63.2^\circ$ ), and TiO<sub>2</sub> NTs ( $2\theta = 26.1^\circ, 38.6^\circ, 48.8^\circ, 54.7^\circ, 55.9^\circ,$  and  $63.5^\circ$ ) associated with the anatase phase are observed in all the XRD patterns<sup>[29, 30]</sup>. These findings demonstrate that the TiO<sub>2</sub> NPs, NWs, NRs, and NTs we synthesized are titania anatase dioxide.

Fig. 3 and Table 1 show the N<sub>2</sub> adsorption isotherm of the the TiO<sub>2</sub> NPs, NWs, NRs, and NTs and the specific surface area are about 91.9122, 116.6744, 126.3625, and 158.8077 m<sup>2</sup>/g, respectively. The large specific surface area for the TiO<sub>2</sub> NRs and NTs, which may be the key factors to absorb more dyes and enhance the performance for FDSSC.

To investigate the effect of TiO<sub>2</sub> morphological changes on dye 719 adsorption capacity, Fig. 4 demonstrates the Ultra-violet (UV)-visible absorption spectra of dye N719 made from the flexible TiO<sub>2</sub> photoanode with different morphologies, which shows three absorption peaks at 308, 373, and 503 nm for the dye N719. The TiO<sub>2</sub> NTs photoanode has the strongest signals, and the orders of the signal strength for the nano TiO<sub>2</sub> are NTs > NRs > NWs > NPs. This result indicates that the TiO<sub>2</sub> NTs photoanode loads more dyes according to the Lam-



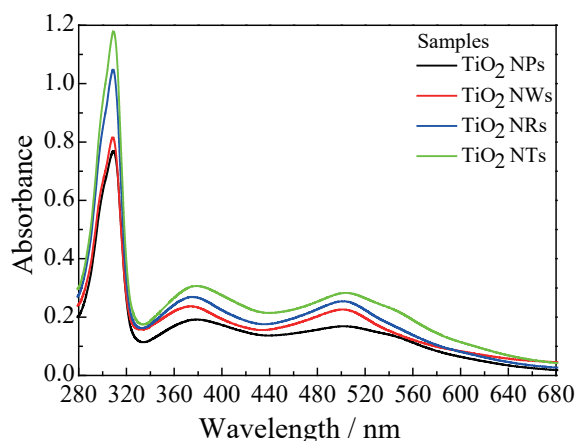


Fig. 4. (Color online) The UV-visible absorption spectra of dye desorbed from TiO<sub>2</sub> films of NPs, NWs, NRs, and NTs.

bert-Beer's law, which means more incident light harvested and the larger photocurrent occurs<sup>[31]</sup>.

Figs. 5(a) and 5(b) are the HRTEM images of TiO<sub>2</sub> NTs with approximate lattice spacing of 2.44–3.71 nm (Fig. 5(c)) and smooth surface, which indicates that most of the P25 particles have been changed into TiO<sub>2</sub> NTs. The length of the TiO<sub>2</sub> NTs is about 100 nm and the diameter is around 15 nm. Fig. 5(d) shows the SAED image of TiO<sub>2</sub> NTs. It can be seen that the TiO<sub>2</sub> NTs are multicrystal structure, and belongs to the (101), (004), and (200) crystal faces for anatase phase.

Figs. 6(a) and 6(b) show the SEM images of the porous PEDOT CE. The PEDOT film with uniform network structure is in favour of improving  $I^-/I_3^-$  electrolyte penetration and enhancing the contact area between CE and electrolyte. Fig. 6(c) shows the CVs of the Pt and PEDOT CEs at the scan rate of 50 mV·s<sup>-1</sup>. The PEDOT CE have a higher current density ( $I_{pc}$ ) absolute value and smaller overpotential ( $V_{pc}$ ) than that of the Pt CE. Both the max anode peak current density ( $I_{pa}$ ) and  $I_{pc}$  are almost unchanged in Fig. 6(d) which indicates a great electrochemical stability for the PEDOT CE<sup>[32]</sup>. This phenomenon signifies that the PEDOT CE possesses the Pt-like electrocatalytic ability for  $I_3^-$  reduction due to the low overpotential loss and highly conductive for the PEDOT CE<sup>[33]</sup>.

Fig. 7 shows the photovoltaic properties of various FDSSCs under the rear illumination of 100 mW·cm<sup>-2</sup> and the detailed parameters are summarized in Table 2. The power conversion efficiencies (PCEs) of the FDSSCs assembled with TiO<sub>2</sub> NTs and the Pt and PEDOT CEs in Fig. 7(a) achieves 5.06% and 7.83%, respectively, which is remarkably higher for the latter than that of the former. This is mainly because the much higher transmittance for the PEDOT CE than that of the Pt CE, and the decrease in incident light intensity via the reflection of Pt CE<sup>[34, 35]</sup>. Fig. 7(b) shows the  $J-V$  curves of the FDSSCs based on the PEDOT CE and the TiO<sub>2</sub> NPs, NWs, NRs, and NTs photoanodes under the rear irradiation. The FDSSCs with the TiO<sub>2</sub> NRs and NTs photoanodes show as high as PCEs of 7.65% and 7.83%, higher than that of the TiO<sub>2</sub> NPs (6.96%) and NWs (7.36%) photoanodes. The distinction in performance of the cells possibly is derived from the differences in electronic transmission of nano TiO<sub>2</sub>. The TiO<sub>2</sub> NRs and NTs with directional structure are more conducive to electronic transmission than that of the TiO<sub>2</sub> NPs and NWs. Simultane-

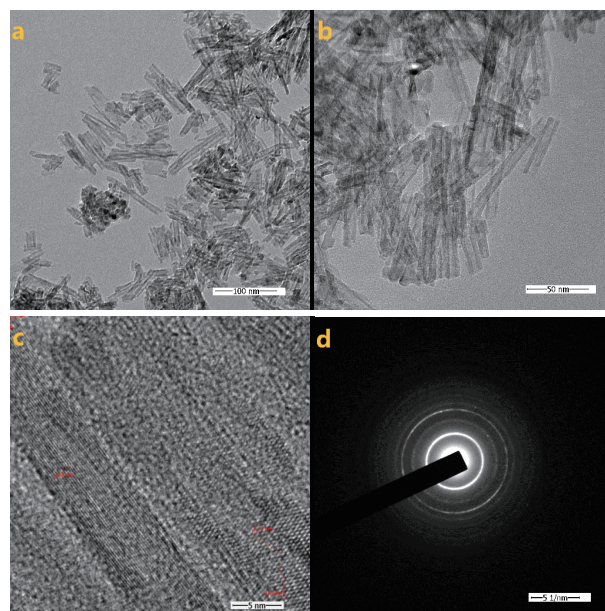


Fig. 5. (a-c) HRTEM images and (d) SAED pattern of the TiO<sub>2</sub> NTs.

ously, the reduction of dye loading capacity on TiO<sub>2</sub> photoanode also plays a certain role for the TiO<sub>2</sub> NPs and NWs.

Fig. 8 presents the Nyquist plots of the devices with TiO<sub>2</sub> NPs, NWs, NRs, and NTs photoanodes and PEDOT CE, in which the performance of devices is directly related to the charge transfer resistance ( $R_{ct1}$  and  $R_{ct2}$ )<sup>[36]</sup>. Because of TiO<sub>2</sub> directional structure could enhance the electron collection efficiency in devices, therefore, the cell based on TiO<sub>2</sub> NTs photoanode shows the lowest values  $R_{ct1}$  of 2.80 Ω·cm<sup>2</sup> and  $R_{ct2}$  of 6.61 Ω·cm<sup>2</sup>, and the other three devices with the TiO<sub>2</sub> NPs, NWs, and NRs photoanodes display the  $R_{ct1}$  of 5.06, 4.17, and 3.59 Ω·cm<sup>2</sup>, and corresponding to the  $R_{ct2}$  of 10.09, 9.56, and 8.31 Ω·cm<sup>2</sup>. The former shows the smallest  $R_{ct1}$  and  $R_{ct2}$  compared to the latter cells. This implies that the TiO<sub>2</sub> NRs and NTs with directional structure for the devices are better for electronic transmission than that of the TiO<sub>2</sub> NPs and NWs, resulting in a higher fill factor (FF) and short-circuit current density. This is in consistent with the results of UV-visible and  $J-V$  photovoltaic performance.

Fig. 9 shows the architecture of a FDSSC with TiO<sub>2</sub> NTs photoanode irradiated from the rear. The function of the TiO<sub>2</sub> blaking layer can reduce the backwash of elections from Ti foil substrate to the electrolyte, thereby enhancing the long-term stability of FDSSC. The TiO<sub>2</sub> NTs provide an unobstructed path for electron transfer, which helps improve the efficiency of charge transfer and electron collection. Moreover, the light emitted from the back can penetrate and be absorbed by the N719 dye very well due to the good transparency of the PEDOT CE, producing more photogenerated charge carriers in FDSSC, and resulting greatly enhanced the short-circuit current density and a superior PCE of 7.83%.

#### 4. Conclusions

An efficient FDSSCs assembled with net-work structure PEDOT CE and TiO<sub>2</sub> NPs, NWs, NRs, and NTs photoanodes achieved power conversion efficiency of 6.96%, 7.36%, 7.65%, and 7.83% under rear illumination of 100 mW·cm<sup>-2</sup>. The morphology of TiO<sub>2</sub> has a significant influence on the photovoltaic performances of FDSSCs. These four FDSSCs with vari-



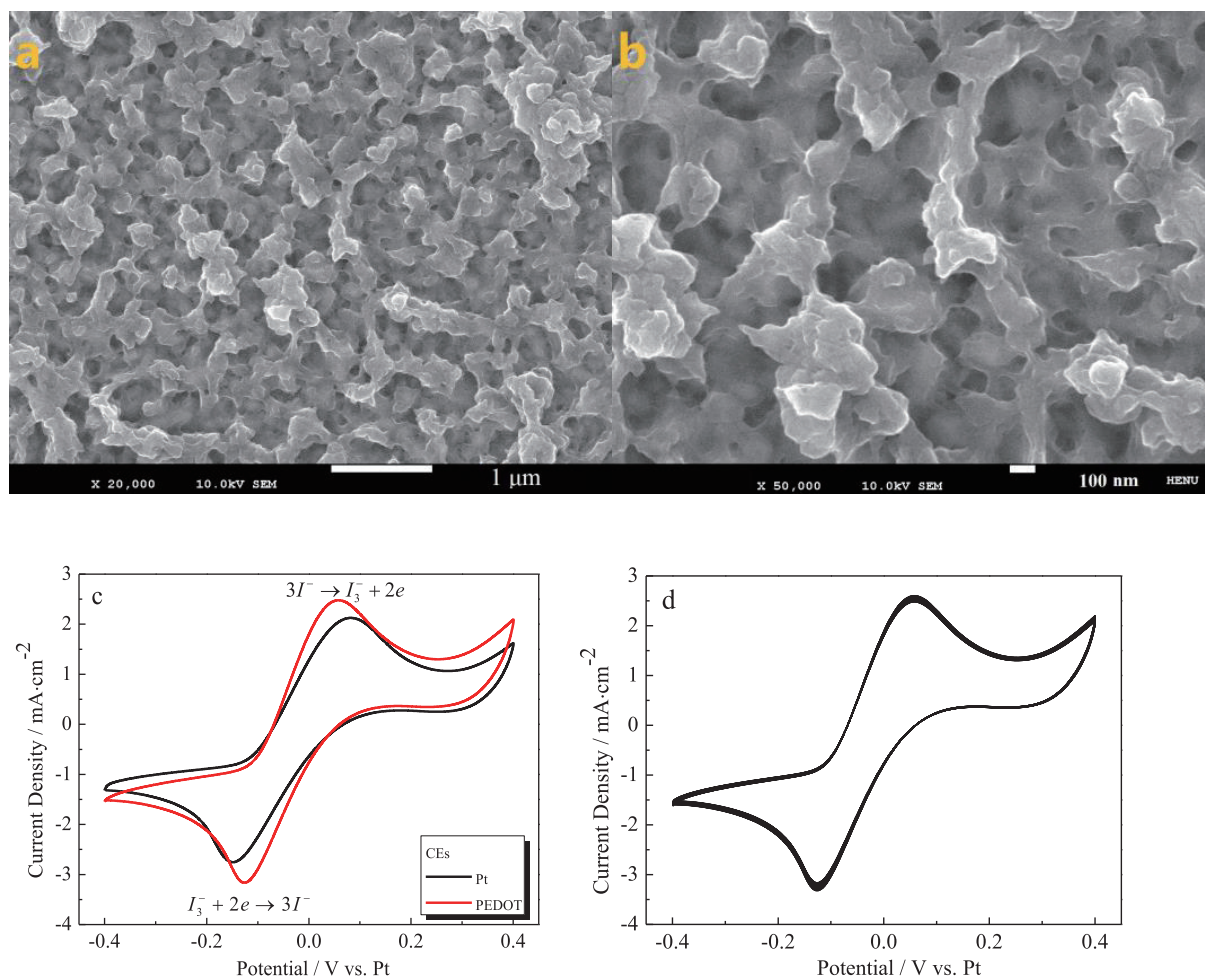


Fig. 6. (Color online) (a, b) SEM images of the porous PEDOT CE; (c) the CVs for the Pt and PEDOT CEs; and (d) the 50 successive CV cycles of the PEDOT CE at the scan rate of  $50 \text{ mV}\cdot\text{s}^{-1}$ .

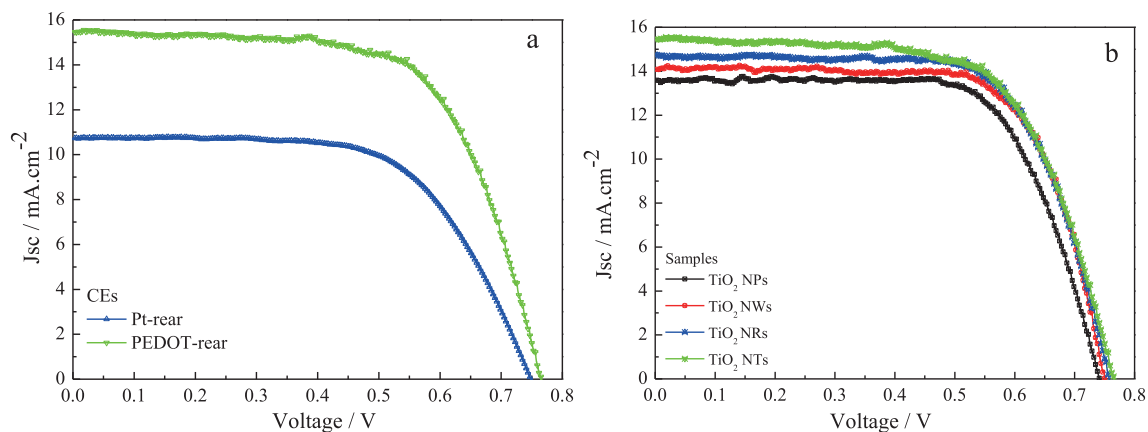


Fig. 7. (Color online)  $J$ - $V$  characteristics of the FDSSCs fabricated with different photoanodes under the standard illumination.

Table 2. The photoelectric properties of the FDSSCs with various CEs and photoanodes.

Devices	CEs	Photoanodes	$V_{oc}$ (V)	$J_{sc}$ ( $\text{mA}\cdot\text{cm}^{-2}$ )	FF	$\eta$ (%)
b	Pt-rear	TiO <sub>2</sub> NTs	0.748	10.74	0.63	5.06
d	PEDOT-rear	TiO <sub>2</sub> NTs	0.766	15.48	0.66	7.83
e	PEDOT-rear	TiO <sub>2</sub> NPs	0.741	13.62	0.69	6.96
f	PEDOT-rear	TiO <sub>2</sub> NWs	0.749	14.24	0.69	7.36
g	PEDOT-rear	TiO <sub>2</sub> NRs	0.757	14.65	0.69	7.65

ous TiO<sub>2</sub> photoanodes morphology possess good fill factor and open circuit voltage, especially for the FDSSCs with TiO<sub>2</sub> NRs and NTs photoanodes, which generate higher short cir-

cuit current density. This is responsible for their oriented structure of NRs and NTs, which are more beneficial to electron and hole transmission in the semiconductor compared to the

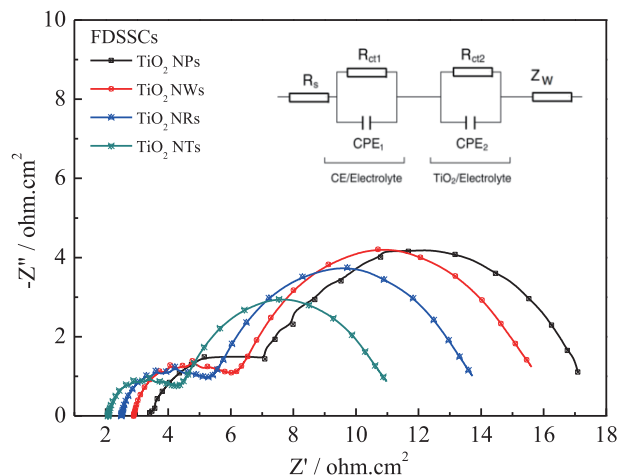


Fig. 8. (Color online) EIS spectra of FDSSCs with the various photoanodes and the relevant equivalent circuit model.

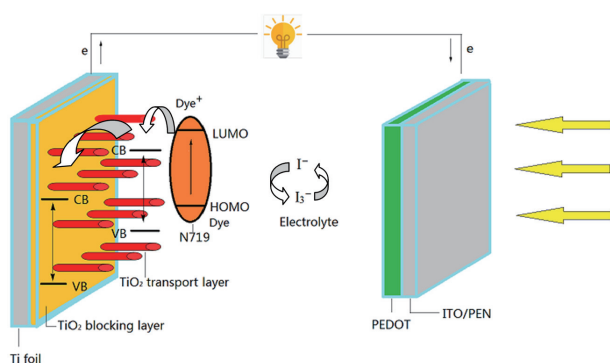


Fig. 9. (Color online) Schematic for a FDSSC based on  $\text{TiO}_2$  NTs photoanode irradiated from the rear.

$\text{TiO}_2$  NPs and NWs photoanodes. This strategy can be further improved by designing a better light-splitting device with vertical incidence and applied other devices with transparent CEs.

## Acknowledgements

The authors are very grateful to the joint support by NSFC (No. 61704047). This work is also supported by Science and Technology Development Project of Henan Province (Nos. 212102210126 and 202300410057).

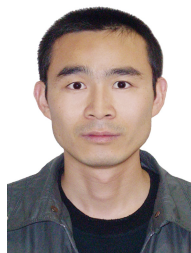
## References

- [1] Briscoe J, Dunn S. The future of using earth-abundant elements in counter electrodes for dye-sensitized solar cells. *Adv Mater Deerfield Beach Fla*, 2016, 28, 3802
- [2] Bellisario D O, Paulson J A, Braatz R D, et al. An analytical solution for exciton generation, reaction, and diffusion in nanotube and nanowire-based solar cells. *J Phys Chem Lett*, 2016, 7, 2683
- [3] Kakiage K, Aoyama Y, Yano T, et al. Highly-efficient dye-sensitized solar cells with collaborative sensitization by silyl-anchor and carboxy-anchor dyes. *Chem Commun*, 2015, 51, 15894
- [4] Huang J Y, He S H, Zhang W Z, et al. Efficient and stable all-inorganic  $\text{CsPbI}_2\text{Br}_2$  perovskite solar cells enabled by dynamic vacuum-assisted low-temperature engineering. *Sol RRL*, 2022, 6, 2100839
- [5] Fujishima A, Honda K. Electrochemical photolysis of water at a semiconductor electrode. *Nature*, 1972, 238, 37
- [6] Hosono E, Matsuda H, Honma I, et al. Synthesis of a perpendicular  $\text{TiO}_2$  nanosheet film with the superhydrophilic property without UV irradiation. *Langmuir*, 2007, 23, 7447
- [7] Han Z T, Li S S, Li J J, et al. Facile synthesis of ZnO nanowires on FTO glass for dye-sensitized solar cells. *J Semicond*, 2013, 34, 074002
- [8] Gapale D L, Bardapurkar P P, Arote S A, et al. Humidity sensing properties of spray deposited Fe doped  $\text{TiO}_2$  thin film. *J Semicond*, 2021, 42, 122805
- [9] Thomas A G, Syres K L. Adsorption of organic molecules on rutile  $\text{TiO}_2$  and anatase  $\text{TiO}_2$  single crystal surfaces. *Chem Soc Rev*, 2012, 41, 4207
- [10] Cai X F, Zhang P, Wei S H. Revisit of the band gaps of rutile  $\text{SnO}_2$  and  $\text{TiO}_2$ : A first-principles study. *J Semicond*, 2019, 40, 092101
- [11] Feng X J, Shankar K, Varghese O K, et al. Vertically aligned single crystal  $\text{TiO}_2$  nanowire arrays grown directly on transparent conducting oxide coated glass: Synthesis details and applications. *Nano Lett*, 2008, 8, 3781
- [12] Liu B, Aydil E S. Growth of oriented single-crystalline rutile  $\text{TiO}_2$  nanorods on transparent conducting substrates for dye-sensitized solar cells. *J Am Chem Soc*, 2009, 131, 3985
- [13] Sadhu S, Jaiswal A, Adyanthaya S, et al. Surface chemistry and growth mechanism of highly oriented, single crystalline  $\text{TiO}_2$  nanorods on transparent conducting oxide coated glass substrates. *RSC Adv*, 2013, 3, 1933
- [14] Sadhu S, Gupta P, Poddar P. Physical mechanism behind enhanced photoelectrochemical and photocatalytic properties of superhydrophilic assemblies of 3D- $\text{TiO}_2$  microspheres with arrays of oriented, single-crystalline  $\text{TiO}_2$  nanowires as building blocks deposited on fluorine-doped tin oxide. *ACS Appl Mater Interfaces*, 2017, 9, 11202
- [15] Ri J H, Wu S F, Jin J P, et al. Growth of a sea urchin-like rutile  $\text{TiO}_2$  hierarchical microsphere film on Ti foil for a quasi-solid-state dye-sensitized solar cell. *Nanoscale*, 2017, 9, 18498
- [16] He S H, Shang L W, Gao Y Y, et al. Holistically modulating charge recombination via trisiloxane surface treatment for efficient dye-sensitized solar cells. *J Alloys Compd*, 2022, 896, 162864
- [17] Fan K, Li R J, Chen J N, et al. Recent development of dye-sensitized solar cells based on flexible substrates. *Sci Adv Mat*, 2013, 5, 1596
- [18] Song L X, Yin X, Xie X Y, et al. Highly flexible  $\text{TiO}_2/\text{C}$  nanofibrous film for flexible dye-sensitized solar cells as a platinum- and transparent conducting oxide-free flexible counter electrode. *Electrochim Acta*, 2017, 255, 256
- [19] He S H, Lan Z, Zhang B, et al. Holistically optimizing charge carrier dynamics enables high-performance dye-sensitized solar cells and photodetectors. *ACS Appl Mater Interfaces*, 2022, 14, 43576
- [20] Gao X M, Shen Z T, Yue G T, et al. Sodium molybdate-assisted synthesis of a cobalt phosphide hybrid counter electrode for highly efficient dye-sensitized solar cells. *ACS Appl Energy Mater*, 2021, 4, 3851
- [21] Du Y, Shen Z, Yue G, et al.  $\text{CoP}@/\text{Ni}_2\text{P}$  microcrystals *in situ* grown on carbon fiber as counter electrode catalysts for high-efficiency dye-sensitized solar cells. *Mater Today Sustain*, 2022, 20, 100262
- [22] He Y, Shen Z T, Yue G T, et al. A dye-sensitized solar cells with enhanced efficiency based on a "pillared effect" of  $\text{CoMoP}_2@/\text{Mxene}@/\text{CNTs}$  composite counter electrode. *J Alloys Compd*, 2022, 922, 166279
- [23] Gao M, Shen Z T, Yue G T, et al. One-pot hydrothermal *in situ* growth of  $\text{In}_4\text{SnS}_8@/\text{MoS}_2@/\text{CNTs}$  as efficient Pt-free counter electrodes for dye-sensitized solar cells. *J Alloys Compd*, 2023, 932, 167643
- [24] Yu F D, Han G S, Tu Y J, et al. Electron extraction mechanism in low hysteresis perovskite solar cells using single crystal  $\text{TiO}_2$  nanorods. *Sol Energy*, 2018, 167, 251
- [25] Lan Z, Xu X X, Zhang X Z, et al. Low-temperature solution-processed efficient electron-transporting layers based on  $\text{BF}_4^-$ -capped  $\text{TiO}_2$  nanorods for high-performance planar perovskite

- solar cells. *J Mater Chem C*, 2018, 6, 334
- [26] Chen W C, Yeh M H, Lin L Y, et al. Double-wall TiO<sub>2</sub> nanotubes for dye-sensitized solar cells: A study of growth mechanism. *ACS Sustainable Chem Eng*, 2018, 6, 3907
- [27] Guo M, Chen J, Zhang J, et al. Coupling plasmonic nanoparticles with TiO<sub>2</sub> nanotube photonic crystals for enhanced dye-sensitized solar cells performance. *Electrochim Acta*, 2018, 263, 373
- [28] Ako R T, Ekanayake P, Lim C M. An analysis of DSSC performance based on nanosphere, nanorod, and nanoparticle anode morphologies. *J Appl Phys*, 2016, 120, 1089
- [29] Liu Y Y, Ye X Y, An Q Q, et al. A novel synthesis of the bottom-straight and top-bent dual TiO<sub>2</sub> nanowires for dye-sensitized solar cells. *Adv Powder Technol*, 2018, 29, 1455
- [30] Qiu Q Q, Li S, Jiang J J, et al. Improved electron transfer between TiO<sub>2</sub> and FTO interface by N-doped anatase TiO<sub>2</sub> nanowires and its applications in quantum dot-sensitized solar cells. *J Phys Chem C*, 2017, 121, 21560
- [31] Xiao Y M, Wu J H, Yue G T, et al. The preparation of titania nanotubes and its application in flexible dye-sensitized solar cells. *Electrochim Acta*, 2010, 55, 4573
- [32] Li K X, Yue G T, Tan F R. A binder-free CF|PANI composite electrode with excellent capacitance for asymmetric supercapacitors. *J Semicond*, 2023, 44, 032701
- [33] Liu X Q, Liang Y, Yue G T, et al. A dual function of high efficiency quasi-solid-state flexible dye-sensitized solar cell based on conductive polymer integrated into poly (acrylic acid-co-carbon nanotubes) gel electrolyte. *Sol Energy*, 2017, 148, 63
- [34] Wu J H, Li Y, Tang Q W, et al. Bifacial dye-sensitized solar cells: A strategy to enhance overall efficiency based on transparent polyaniline electrode. *Sci Rep*, 2014, 4, 4028
- [35] Du Y, Yue G T, Lan Z, et al. A dye-sensitized solar cell based on magnetic CoP@FeP<sub>4</sub>@Carbon composite counter electrode generated an efficiency of 9.88%. *Inorg Chem Front*, 2021, 8, 5034
- [36] Tang Q W, Zhu W L, He B L, et al. Rapid conversion from carbohydrates to large-scale carbon quantum dots for all-weather solar cells. *ACS Nano*, 2017, 11, 1540



**Zhe He** received his BS degree in 2022 after graduating from Henan Normal University. Now he is a master's student at Henan University. Since September 2022, he has been working in Prof. Furui Tan's research group under the supervision of Associate Professor Gentian Yue. His current research focuses on DSSC and supercapacitors.



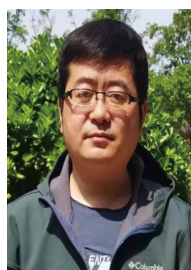
**Gentian Yue** received his Ph.D. degree from Huaqiao University, China in 2013. Since then, he has been working as a full time associate professor at Henan Key Laboratory of Photovoltaic Materials, Henan University, China. His research interests include material synthesis and device fabrication of dye sensitized solar cells, supercapacitor, and energy capture and storage devices for wearable electronics.



**Yueyue Gao** received his master's degree in Chemical Engineering and Technology from Qiqihar University, China in 2014. And he received his Ph.D. degree from School of Chemistry and Chemical Engineering, Harbin Institute of Technology (HIT), China in 2018. Since then, he joined Henan Key Laboratory of Photovoltaic Materials, Henan University, China in 2018. His research interest mainly focuses on the design, synthesis and performance study of furan-based organic photovoltaic materials.



**Chen Dong** received his Ph.D. degree from Lanzhou Institute of Chemical Physics, Chinese Academy of Sciences (CAS), under the supervision of Prof. Xiuxun Han and Prof. Jinqing Wang. Since then, he joined Henan Key Laboratory of Photovoltaic Materials, Henan University, China in 2019. His research interest is all-inorganic perovskite solar cells.



**Furui Tan** is currently an professor in the Henan Key Laboratory of Photovoltaic Materials, Henan University, China. He received his Ph.D. degree from Institute of Semiconductors, Chinese Academy of Sciences (ISCAS) in 2011. He joined the Sargent group in the Department of Electronics and Computer Engineering (ECE) in the University of Toronto, as a visiting scholar in June 2017 and June 2018. His research group focuses on organic and nanoscale materials for solar cells, photodetectors, and electro-catalysis etc.